In vivo targeted magnetic resonance imaging and visualized photodynamic therapy in deep-tissue cancers using folic acid-functionalized superparamagnetic-upconversion nanocomposites†

Leyong Zeng,[a,b] Lijia Luo,[a] Yuanwei Pan,[a] Song Luo,[b] Guangming Lu*[b,c] and Aiguo Wu*[a]

Multifunctional nanoprobes used in magnetic resonance imaging (MRI) and photodynamic therapy (PDT) also have potential applications in diagnosis and visualized therapy of cancers, and hence it is important to investigate the active-targeting ability and *in vivo* reliability of these nanoprobes. In this work, folic acid (FA)-targeted, photosensitizer (PS)-loaded Fe_3O_4@$NaYF_4$:Yb/Er (FA-NPs-PS) nanocomposites were synthesized for *in vivo* T_2-weighted MRI and visualized PDT of cancers by modeling MCF-7 tumor-bearing nude mice. By measuring the upconversion luminescence (UCL) and fluorescence emission spectra, the as-prepared FA-NPs-PS nanocomposites showed near-infrared (NIR)-triggered PDT performance due to the production of a singlet oxygen species. Moreover, by tracing PS fluorescence in MCF-7, HeLa cells and in MCF-7 tumors, the FA-targeted nanocomposites demonstrated good targeting ability both *in vitro* and *in vivo*. Under the irradiation of a 980 nm laser, the viabilities of MCF-7 and HeLa cells incubated with FA-NPs-PS nanocomposites could decrease to about 18.4% and 30.7%, respectively, and the inhibition of MCF-7 tumors could reach about 94.9%. The transverse MR relaxivity of 63.79 mM^{-1} s^{-1} (r_2 value) and *in vivo* MR imaging of MCF-7 tumors indicated an excellent T_2-weighted MR performance. This work demonstrated that FA-targeted MRI/PDT nanoprobes are effective for *in vivo* diagnosis and visualized therapy of breast cancers.

1. Introduction

Multifunctional nanoprobes for magnetic resonance imaging (MRI) and photodynamic therapy (PDT) have shown potential applications in diagnosis and visualized therapy of cancers due to the advantages of being non-radiative and non-invasive. In addition, photosensitizers (PS), as light-driven drugs, also play a key role in the PDT of cancers. Many nanomaterials, such as carbon nanodots, gold nanorods, graphene and upconversion luminescence (UCL) nanomaterials, have been investigated as carriers of PS and have shown to improve the PDT performance as well as the imaging performance.[1–4] Moreover, magnetic nanomaterials were also used to load PS for simultaneous MRI and PDT.[5–8] In previous reports, multifunctional nanoprobes of MRI/PDT were usually organic PS-loaded superparamagnetic/paramagnetic nanomaterials for T_1- or T_2-weighted MRI and visible-triggered organic PDT[5–12] and inorganic PS-loaded superparamagnetic nanomaterials for MRI and visible/ultraviolet (UV)-triggered inorganic PDT.[13,14]

At present, the clinical use of PDT is restricted due to its weak penetration into deep tissues and non-specific damage to normal tissues. It is known that visible/ultraviolet (UV) light (about 400–700 nm) has weak penetration, only a few millimeters, but near-infrared (NIR) radiation (about 700–1100 nm) has deep penetration into tissues, by one to several centimeters.[15–18] The targeting strategy of nanoprobes is critical to improve their selectivity in imaging and therapy of cancers, which could reduce the non-specific damage.[19] Folic acid (FA) is one of the most popular targeting ligands as it

[a]Key Laboratory of Magnetic Materials and Devices & Division of Functional Materials and Nanodevices, Ningbo Institute of Materials Technology and Engineering, Chinese Academy of Sciences, Ningbo 315201, P. R. China. E-mail: aiguo@nimte.ac.cn; Fax: +86 574 86685163; Tel: +86 574 86685039
[b]Department of Medical Imaging, Jinling Hospital, School of Medicine, Nanjing University, Nanjing 210002, P. R. China. E-mail: cjr.luguangming@vip.163.com; Fax: +86 25 84804659; Tel: +86 25 80860185

could have high specificity to breast and cervical tumors, in which the FA receptor is over-expressed.[26] By coupling targeting ligands with nanoprobes, the specific uptake of tumors can be increased and the non-specific damage of normal tissues decreased.[20–24] Recently, due to the excellent properties of UCL nanomaterials in MRI/fluorescence imaging,[25,26] magnetic-upconversion nanocomposites with different structures and performances have been synthesized and widely investigated[27] and are promising as a type of theranostic system for deep-tissue diagnosis, visualized therapy, and also for the prognosis assessment of cancers.[24,28–32] The synthesis of PS-loaded Gd-based upconversion nanocomposites, T_1-weighted MRI and NIR-triggered PDT, has been previously reported, which demonstrated the simultaneous MRI and deep-tissue PDT *in vitro* and *in vivo*.[33–37] On considering the good biocompatibility of superparamagnetic iron oxide nanoparticles, superparamagnetic-upconversion nanocomposites have been synthesized by a silica-assisted method, and they were also investigated for MRI and fluorescent imaging.[29,38–42] However, it was found to be more interesting to design photosensitizer-loaded iron oxide-UCL nanocomposites for T_2-weighted MRI and NIR-triggered visualized PDT in deep-tissue tumors. Furthermore, *in vivo* biocompatibility and *in vivo* reliability of nanoprobes were the basis of clinical applications. Therefore, to improve safety and selectivity, it was important to develop targeted nanoprobes of MRI and NIR-triggered visualized PDT and simultaneously investigate *in vivo* reliability in deep-tissue cancers.

In this study, we report the synthesis of FA-targeted, photosensitizer (PS)-loaded $Fe_3O_4@NaYF_4$:Yb/Er (FA-NPs-PS) nanocomposites *via* direct coupling and their applications for *in vivo* targeted T_2-weighted MRI and visualized PDT in deep-tissue cancers. Singlet oxygen was measured, and *in vitro* PDT was characterized for MCF-7 and HeLa cells under the excitation of a 980 nm laser. Moreover, by tracing PS fluorescence, the targeting ability of FA was assessed both *in vitro* and *in vivo*. Finally, by modeling MCF-7 tumor-bearing nude mice, *in vivo* MRI and PDT performance of FA-NPs-PS nanocomposites were investigated. This work provided new insight for targeting and *in vivo* reliability of MRI/PDT nanoprobes and will be helpful for developing new theranostic systems in targeted diagnosis and visualized therapy of deep-tissue cancers.

2. Experimental section

2.1 Chemicals and materials

Ferric acetylacetonate ($Fe(acac)_3$), rare-earth oxides (Y_2O_3, Yb_2O_3, Er_2O_3), trifluoroacetic acid (CF_3COOH), sodium carbonate (Na_2CO_3) and 3-aminopropyltriethoxysilane (APTS) were purchased from Aladdin Industrial Inc. (Shanghai, China). Oleylamine (OM), *n*-octyl alcohol, polyethylene glycol (PEG, MW = 1500) and folic acid (FA) were purchased from Sinopharm Chemical Reagents Co. Ltd (Shanghai, China). Tetrasulfonic phthalocyanine aluminium ($AlPcS_4$) organic photosensitizer and 9,10-anthracenediyl-bis(methylene)dimalonic

acid (ABDA) were purchased from J&K Scientific Ltd (Shanghai, China). 5-Diphenyl-2-*H*-tetrazolium bromide (MTT), 1-ethyl-3-(3′-dimethylaminopropyl) carbodiimide (EDC), *N*-hydroxysuccinimide (NHS), Dulbecco's modified Eagle's medium (DMEM) and fetal bovine serum (FBS, Gibco) were purchased from Keygen Biotech Co. Ltd (Nanjing, China). Calcein acetoxymethyl ester (CAM) and ethidium homodimer-1 (EthD-1) were purchased from Life Technologies (Shanghai, China). All the chemicals were used as received without further purification.

2.2 Synthesis and characterization of nanocomposites

Fe_3O_4-$NaYF_4$:Yb/Er nanoparticles (NPs), FA-targeted NPs (FA-NPs) and PS-loaded FA-NPs (FA-NPs-PS) were firstly synthesized. The transmission electron microscopy (TEM) images were taken using a Tecnai F20 transmission electron microscope operated at 200 kV. The dynamic light scattering (DLS) spectra were obtained using a Brookhaven ZetaPALS Analyzer. The $M–H$ curves were measured by Quantum Design Model-9 physical performance measurement system (PPMS). The UV-vis absorption spectra were obtained by a PerkinElmer Lambda 35 UV-vis spectrophotometer. The fluorescent emission spectra and UCL spectra were measured by a Hitachi F4600 fluorescent spectrophotometer. MR imaging and relaxivity performance were tested by a 3.0 T clinical MR instrument (Siemens Trio) and Mico MR analyzing system (Shanghai Niumag Corporation) with a magnetic field of 0.47 T, respectively. The cell viabilities in the MTT assay were measured by a BioTek ELX 800 microplate reader. The live/dead cell staining and the Hematoxylin and Eosin (H&E) staining were examined using a Leica DMI 3000 fluorescent microscope. The fluorescence imaging of $AlPcS_4$ photosensitizers in cells and in tumors was carried out using a IVIS Lumina animal imaging system (Xenogen Corporation-Caliper, USA).

2.3 *In vitro* MRI and PDT

For *in vitro* MRI measurement, MCF-7 and HeLa cells in logarithmic growth were cultured in 6-well plates for 24 h and then were incubated with NP-PS and FA-NPs-PS, in which the concentrations of different nanoparticles were 0, 50, 100, 150, 200, and 250 μg mL^{-1}. After another 24 h, the MCF-7 and HeLa cells were washed with PBS three times, digested and collected by centrifugation. Finally, they were dispersed in 1 mL of 1% agarose for the T_1- and T_2-weighted MR imaging in the 3.0 T clinical MR instrument. Furthermore, T_1- and T_2-weighted MR imaging and relaxivity of NP-PS and FA-NPs-PS were also measured, respectively.

For *in vitro* PDT measurements, MCF-7 and HeLa cells in logarithmic growth were cultured in 96-well plates for 24 h, and then were incubated with NPs, FA-NPs, NP-PS, and FA-NPs-PS for another 24 h, in which the concentrations of different nanoparticles were 0, 50, 100, 150, 200, and 250 μg mL^{-1}. After 4 h, the cells were irradiated by a 980 nm laser with a power density of 0.5 W cm^{-2} for 0, 1, 4, 7, and 10 min, respectively. After another 20 h, the viabilities were measured by the MTT assay. Furthermore, the viabilities of MCF-7 and

HeLa cells, as control experiments, were measured after irradiation by a 980 nm laser.

2.4 *In vivo* MRI and PDT

For *in vivo* MRI measurements, MCF-7 tumor-bearing nude mice were intratumorally injected with 100 μL of FA-NPs-PS (500 μg mL^{-1} in PBS), and the T_1- and T_2-weighted MR imaging was measured 2 h before and 2 h after the injection. Furthermore, MCF-7 tumor-bearing nude mice were also injected with 100 μL of PBS, free PS (12.5 μg mL^{-1} in PBS), NPs-PS (500 μg mL^{-1} in PBS), and FA-NPs-PS (500 μg mL^{-1} in PBS) *via* the tail vein, and then the PS fluorescence imaging of tumor, heart, liver, spleen, lung, and kidney in different mice was undertaken using an animal imaging system.

For *in vivo* PDT measurements, MCF-7 tumor-bearing nude mice were randomly divided into 4 groups ($n = 6$, per group). The tumor-bearing nude mice were intratumorally injected and irradiated with 100 μL of PBS, PBS + NIR, FA-NPs-PS (500 μg mL^{-1} in PBS), FA-NPs-PS + NIR (500 μg mL^{-1} in PBS), for groups 1, 2, 3, and 4, respectively. In particular, the mice in groups 2 and 4 were irradiated by a 980 nm laser with a power density of 0.5 W cm^{-2} for 10 min on the second day after the injection. The tumor volume and body weight were measured every other day, and the volume was calculated to be length × width × width/2. On the fifteenth day, the mice were sacrificed, and the tumors and the major organs (heart, liver, spleen, lung, and kidney) were dissected for H&E staining. For the MCF-7 tumor-bearing nude mice in groups 3 and 4, the PS fluorescence imaging was recorded between 15 day treatments.

2.5 Statistical analysis

Data were expressed as mean ± standard deviation (SD). Statistical differences were analyzed by the Student's *t* test. A value of $p < 0.05$ was taken as statistically significant.

3. Results and discussion

3.1 Synthesis and characterization of FA-NPs-PS nanocomposites

Fig. 1 shows the synthesis schematic of FA-NPs-PS nanocomposites for simultaneous T_2-weighted MRI and PDT of breast cancers. The as-prepared core–shell Fe$_3$O$_4$@NaYF$_4$:Yb/Er nanoparticles were modified with PEG, APTS, FA targeting ligands, and loaded with PS. The obtained FA-NPs-PS nanocomposites were applied as targeted theranostic nanoprobes for *in vivo* T_2-weighted MRI and NIR-triggered PDT of breast cancers under the irradiation of a 980 nm laser.

In order to investigate the application of FA-NPs-PS nanocomposites in MRI and PDT of cancers, the physicochemical properties of different nanoparticles were firstly characterized. Fig. 2(a) shows DLS curves of different nanoparticles, in which the average size of NPs, FA-NPs, and FA-NPs-PS was 129, 147, and 175 nm, respectively, and the inset shows the TEM image of core–shell Fe$_3$O$_4$@NaYF$_4$:Yb/Er nanoparticles. The slight increase of nanocomposite size from NPs, FA-NPs to FA-NPs-PS could be attributed to the change of surface potential, which was measured to be 37.1 mV, 16.8 mV and 12.5 mV, respectively (Fig. S1†). Fig. 2(b) shows the UV-vis absorbance spectra of NPs, FA-NPs, and FA-NPs-PS. In the UV-vis spectra of FA-NPs and FA-NPs-PS, a wide absorbance band located at about 380 nm and two absorbance peaks located at about 630 and 670 nm are observed, respectively. Based on UV-vis absorbance spectra of free FA and free PS (Fig. S2†), the wide band located at 380 nm could be attributed to FA, and the peaks located at 630 and 670 nm could be attributed to PS. In the inset of Fig. 2(b), the color change of different colloids also indicated that the FA and PS were successfully coupled and loaded. Fig. 2(c) shows the *M–H* curves for different nanoparticles, in which the saturation magnetization of NPs, FA-NPs and FA-NPs-PS was 15.6, 14.8, and 14.0 emu g^{-1},
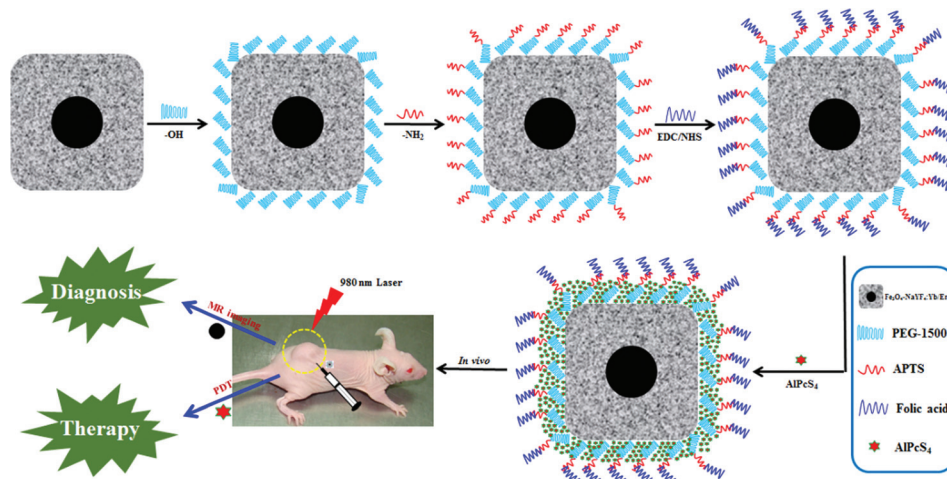
Fig. 1 Schematics of bi-functional theranostic nanoprobes based on FA-targeted photosensitizer-loaded Fe$_3$O$_4$@NaYF$_4$:Yb/Er nanocomposites.
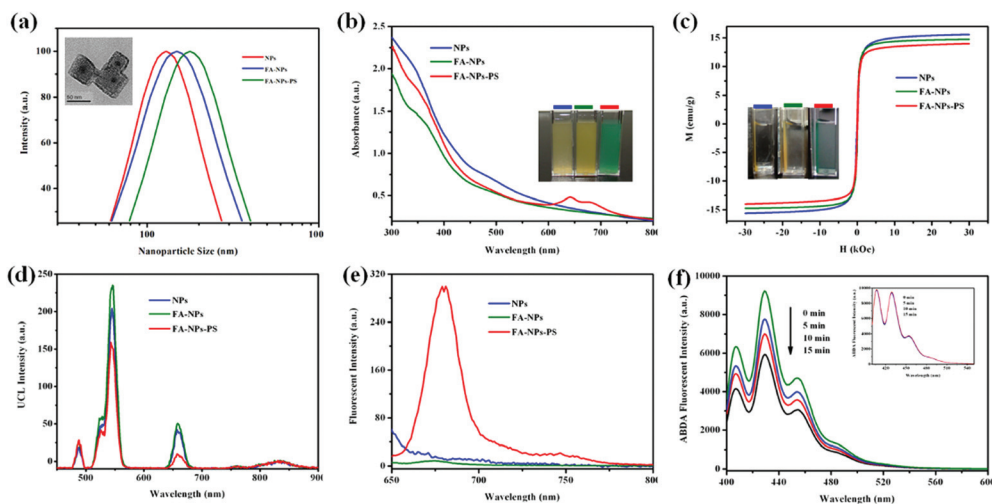
Fig. 2 Size distribution, UV-vis absorbance spectra, $M-H$ curves, UCL spectra, and fluorescent spectra of NPs, FA-NPs and FA-NPs-PS nanocomposites. (a) DLS size distribution, and TEM image is shown in the inset; (b) UV-vis absorbance spectra, and the corresponding real images of colloids are shown in the inset; (c) $M-H$ curves, and the corresponding real images of colloids are shown in the inset; (d) UCL spectra under the excitation of 980 nm laser; (e) fluorescent emission spectra with an excitation wavelength of 633 nm; (f) singlet oxygen detection of FA-NPs-PS under the irradiation of a 980 nm laser for different times by measuring the fluorescent emission spectra of ABDA with the excitation wavelength of 380 nm.

respectively, and the real images of magnetic separation also demonstrated good magnetism of different nanoparticles.

UCL and the production of a singlet oxygen species were both important factors to investigate NIR-triggered PDT of PS-loaded UCL nanomaterials. Fig. 2(d) shows the UCL spectra of NPs, FA-NPs and FA-NPs-PS under the irradiation of a 980 nm laser, in which three main UCL bands located at about 545, 659 and 488 nm were observed, respectively. Moreover, the fluorescent emission peak located at about 678 nm indicated a strong emission of photosensitizers in the FA-NPs-PS sample, as shown in Fig. 2(e). By reacting ABDA and FA-NPs-PS under the irradiation of a 980 nm laser, the fluorescent emission spectra of ABDA were measured. As shown in Fig. 2(f), the peak intensity of ABDA fluorescent emission gradually decreased by increasing the irradiation time from 0 to 15 min, which indicated that the singlet oxygen species could be produced under the irradiation of a 980 nm laser. However, by reacting ABDA and free PS under the irradiation of a 980 nm laser, the peak intensity of ABDA did not decrease, indicating that no singlet oxygen species was produced. The results indicated that the as-prepared FA-NPs-PS nanocomposites could have good PDT performance for cancers.

3.2　*In vitro* and *in vivo* biocompatibility study

To prove the safety of FA-NPs-PS nanocomposites, the *in vitro* and *in vivo* biocompatibility was investigated by the MTT assay and H&E staining, respectively. Fig. 3(a) and (b) show the viabilities of MCF-7 and HeLa cells incubated with NPs, FA-NPs, NPs-PS, and FA-NPs-PS with different concentrations. It was observed that the viabilities were higher than 88% for MCF-7 cells and higher than 87% for HeLa cells. Moreover, in all nanoparticles, cell viabilities incubated with FA-NPs-PS

were the lowest, which could be attributed to the toxicity of PS and the excessive uptake of nanoparticles due to FA targeting. Fig. 3(c) shows the H&E staining images of the major organs of healthy nude mice injected with PBS and FA-NPs-PS *via* the tail vein. No evident tissue lesion was observed in histological specimens of the two experimental groups. The fibrosis of the heart and lungs was not observed, the inflammatory reaction of the liver was not found, the glomerular and tubular in the kidneys were clearly displayed, and the structure of the intestinal villus was clearly present in the intestine. The *in vitro* and *in vivo* biocompatibility indicated that the as-prepared FA-NPs-PS nanocomposites could be safe for possible applications in MRI and PDT of cancers.

3.3　*In vitro* and *in vivo* MRI study

The *in vitro* and *in vivo* MR performances were investigated by measuring the longitudinal and transverse MR relaxivity and the T_1- and T_2-weighted MR imaging. Fig. 4(a) shows the longitudinal (r_1) and transverse (r_2) relaxivity curves of FA-NPs and FA-NPs-PS, in which the r_1 and r_2 values were 1.74 mM^{-1} s^{-1}, 48.42 mM^{-1} s^{-1} for FA-NPs and 2.02 mM^{-1} s^{-1}, 63.79 mM^{-1} s^{-1} for FA-NPs-PS. By loading PS, the improvement of the r_2 value might be related to the better stability of FA-NPs-PS nanocomposites. Moreover, as shown in Fig. 4(b), the T_1- and T_2-weighted MR images of the nanoparticles and their incubation cells were also characterized, in which the T_2-weighted MR images got darker. Fig. 4(c) and (d) show the *in vivo* T_2-weighted MR images of MCF-7 tumor-bearing nude mouse 2 h before and after the injection, in which the tumor section obviously got darker after the injection. The *in vitro* and *in vivo* MR results demonstrate that the as-prepared FA-NPs-PS nano-
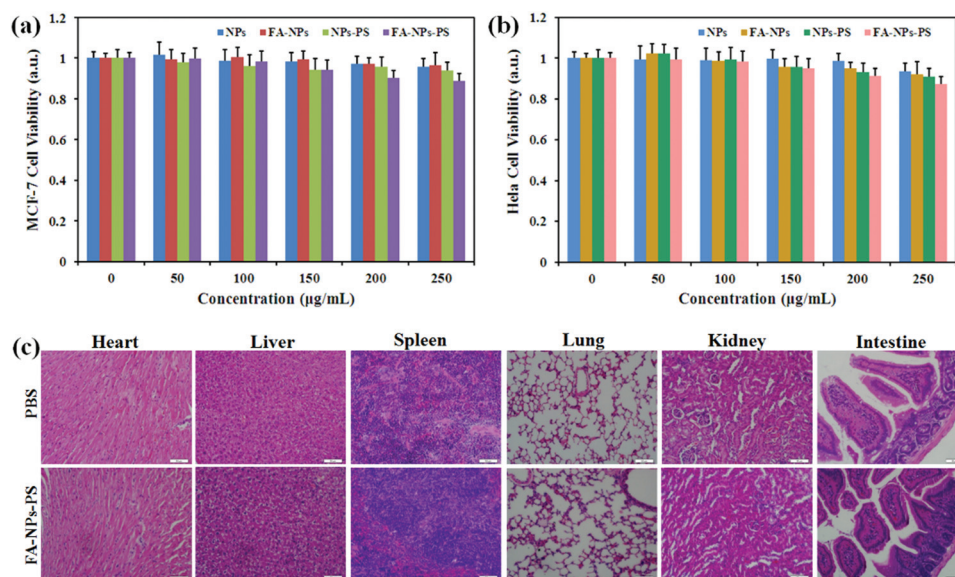
Fig. 3 *In vitro* and *in vivo* toxicity of nanocomposites by the MTT assay and H&E staining. (a) Viabilities of MCF-7 cells incubated with NPs, FA-NPs, NPs-PS, and FA-NPs-PS. (b) Viabilities of HeLa cells incubated with NPs, FA-NPs, NPs-PS, and FA-NPs-PS. (c) H&E staining images of major organs (heart, liver, spleen, lung, kidney, and intestine) of healthy nude mice injected with PBS and FA-NPs-PS *via* the tail vein.
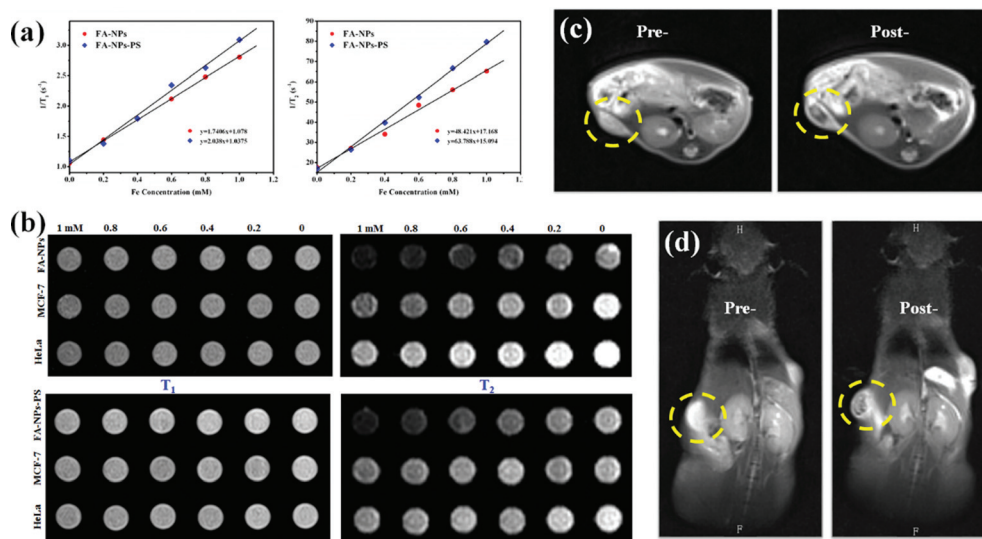

Fig. 4 *In vitro* and *in vivo* MR performance characterization. (a) Longitudinal (r_1) and transverse (r_2) MR relaxivity curves of FA-NPs and FA-NPs-PS nanocomposites; (b) T_1- and T_2-weighted MR images of FA-NPs, FA-NPs-PS nanocomposites and MCF-7 and HeLa cells incubated with FA-NPs and FA-NPs-PS nanocomposites, respectively; (c) and (d) T_2-weighted MR images of MCF-7 tumor-bearing nude mice before and after injection of FA-NPs-PS.

composites could have potential applications as T_2-weighted MRI contrast agents.

3.4 *In vitro* PDT performance

Under the irradiation of a 980 nm laser, the *in vitro* PDT performance was assessed by the MTT assay and live/dead cell staining. Fig. 5(a) and (b) show the viabilities of MCF-7 and HeLa cells in control experiments and incubated with NPs-PS

and FA-NPs-PS on increasing the irradiation time from 0 to 10 min. By FA targeting, a significant number of the incubated cells were killed, and the viabilities of MCF-7 and HeLa cells decreased to 18.4% and 30.7%, respectively, compared with 25.7% and 34.4% on incubation with NPs-PS. Moreover, the viabilities of MCF-7 and HeLa cells in the control experiments only decreased to 93.9% and 91.3%, respectively, indicating that a single 980 nm laser has low photo-damage for cells.
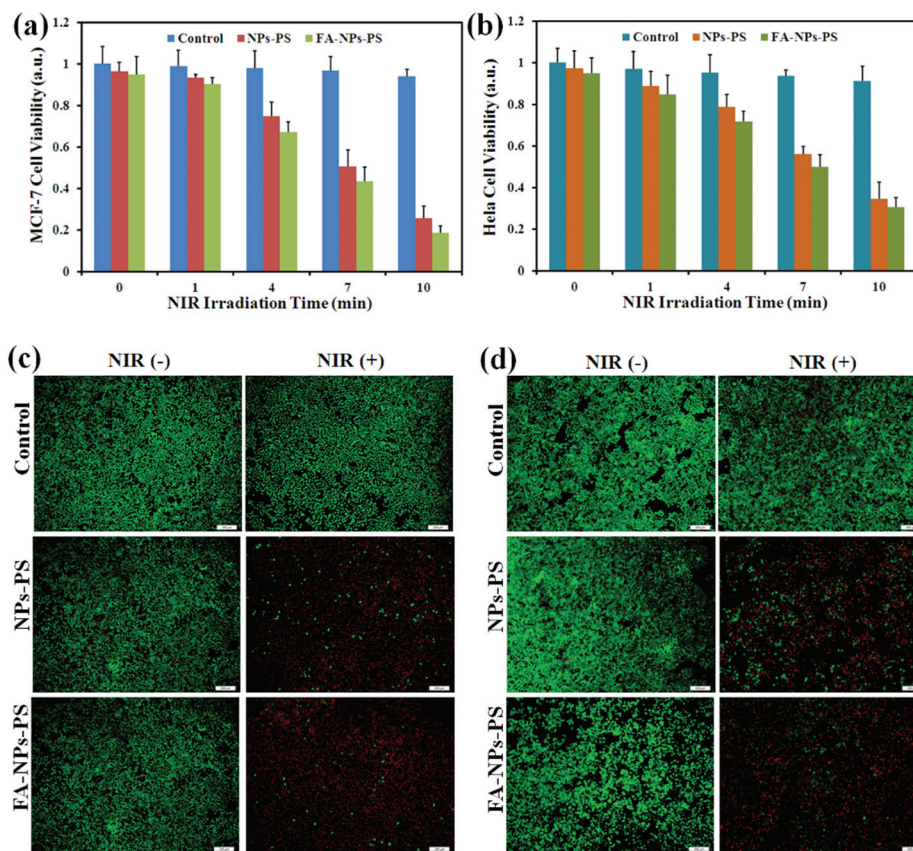
Fig. 5 *In vitro* PDT performance of MCF-7 and HeLa cells incubated with NPs-PS and FA-NPs–PS, respectively, and characterized by the MTT assay and live/dead cell staining under the irradiation of a 980 nm laser with a power density of 0.5 W cm^{-2}. (a) and (b) Viabilities of MCF-7 (a) and HeLa (b) cells in control experiments and incubated with NPs-PS and FA-NPs-PS nanocomposites with the irradiation time of 0, 1, 4, 7, and 10 min; (c) and (d) live/dead cell staining images of MCF-7 (c) and HeLa (d) cells in control experiments and incubated with NPs-PS and FA-NPs-PS by CAM/EthD-1 staining method under the irradiation of a 980 nm laser with a power density of 0.5 W cm^{-2} and the irradiation time of 10 min (the scale bar is 200 μm).

Fig. 5(c) and (d) show the result of cell staining under different conditions, in which live/dead cells were labeled in green/red colors. Being consistent with that of the MTT assay, more MCF-7 and HeLa cells could be killed by incubating with FA-targeted NPs-PS. The *in vitro* PDT demonstrated that a significant number of the incubated cells could be killed using the combination of FA targeting and NIR irradiation.

3.5 Cellular uptake and fluorescence tracing

The cellular uptake and targeted assessment of FA-NPs-PS in cells and in tumors were investigated by TEM and PS fluorescence imaging. Fig. 6(a)–(c) show fluorescence images of FA-NPs-PS nanocomposites and their incubation cells at different concentrations. Compared with pure FA-NPs-PS nanocomposites, the PS fluorescence intensity in cells got weaker, which was attributed to the partial uptake of FA-NPs-PS nanocomposites by the cells. Moreover, the fluorescence intensity in MCF-7 cells was stronger than in HeLa cells, indicating a better targeting ability for MCF-7 cells. In addition, the cellular uptake of nanocomposites was also characterized by Bio-TEM. Fig. 6(d) and (e) show TEM images of MCF-7 and HeLa cells

incubated with FA-NPs-PS nanocomposites. Many nanocomposites accumulated in vesicles, and the accumulation was more significant in MCF-7 cells, which is also consistent with the fluorescence images. Moreover, in order to quantitatively characterize the *in vitro* targeting ability of FA, the flow cytometer assay of MCF-7 cells and HeLa cells incubated with NPs-PS and FA-NPs-PS nanocomposites was measured by detecting PS fluorescence, which indicated that the FA-NPs-PS nanocomposites greatly promoted the uptake of PS in both MCF-7 and HeLa cells (Fig. S4 and S5†).

Furthermore, the targeting ability of FA in MCF-7 tumor-bearing nude mice was assessed through the intravenous injection of PBS, free PS, NPs-PS and FA-NPs-PS *via* the tail vein, by measuring the PS fluorescence intensity of the tumor and major organs (heart, liver, spleen, lung and kidney) in different mice. As shown in Fig. 6(f) and (g), by injecting NPs-PS and FA-NPs-PS, the nanocomposites mainly accumulated in the liver and tumor due to the extra uptake of Kupffer cells in the liver and the enhanced permeation and retention (EPR) effect of nanomaterials in the tumor. Moreover, more nanocomposites were taken up by the tumor following injection
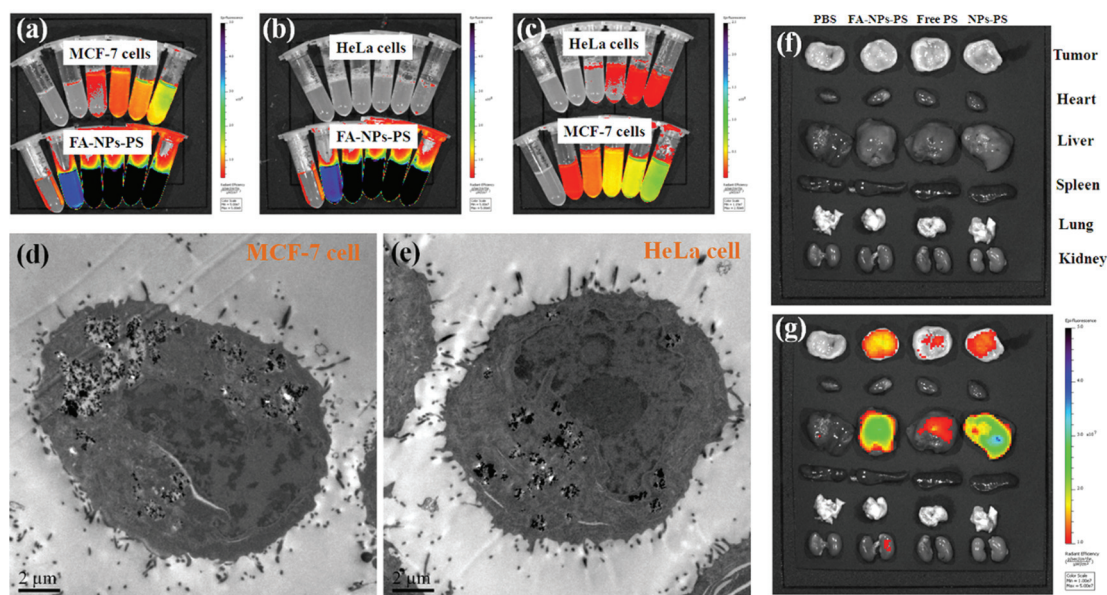
Fig. 6 Cellular uptake and *in vivo* bio-distribution of FA-NPs-PS nanocomposites characterized by fluorescent imaging and Bio-TEM. (a) Fluorescent images of FA-NPs-PS (bottom) and MCF-7 cells incubated with FA-NPs-PS (top); (b) fluorescent images of FA-NPs-PS (bottom) and HeLa cells incubated with FA-NPs-PS (top); (c) fluorescent images of MCF-7 cells (bottom) and HeLa cells incubated with FA-NPs-PS (top), respectively; (d) and (e) cellular uptakes of MCF-7 cells (d) and HeLa cells (e) incubated with FA-NPs-PS, respectively; (f) real images of tumors and major organs of MCF-7 tumor-bearing nude mice; and (g) fluorescent images of tumors and major organs of MCF-7 tumor-bearing nude mice injected with PBS, FA-NPs-PS, NPs-PS, and free PS *via* the tail vein.

with FA-NPs-PS, which could be attributed to FA targeting, as well as the EPR effect. Furthermore, in order to quantitatively investigate the *in vivo* targeting ability of FA, the *in vivo* biodistribution of FA-NPs-PS nanocomposites (in tumor, heart, liver, spleen, lung and kidney) *via* an intravenous injection was also measured, which indicated that FA-NPs-PS nanocomposites accumulate to a greater extent in the tumor, excluding the liver and spleen (Fig. S6†).

3.6 *In vivo* PDT performance

By intratumorally injecting FA-NPs-PS nanocomposites, the volume change of MCF-7 tumors was traced by measuring the

PS fluorescence over 15 day treatments. Fig. 7(a) and (b) show the fluorescence images of MCF-7 tumor-bearing nude mice in groups of FA-NPs-PS and FA-NPs-PS + NIR, respectively. By injecting FA-NPs-PS nanocomposites, the PS fluorescence intensity did not decrease over 15 days. However, under the irradiation of a 980 nm laser, the PS fluorescence intensity gradually got weaker, and even disappeared, which indicated that the volume of the MCF-7 tumor got smaller; in addition, the photo-bleach of PS was also occurring during the process of PDT.

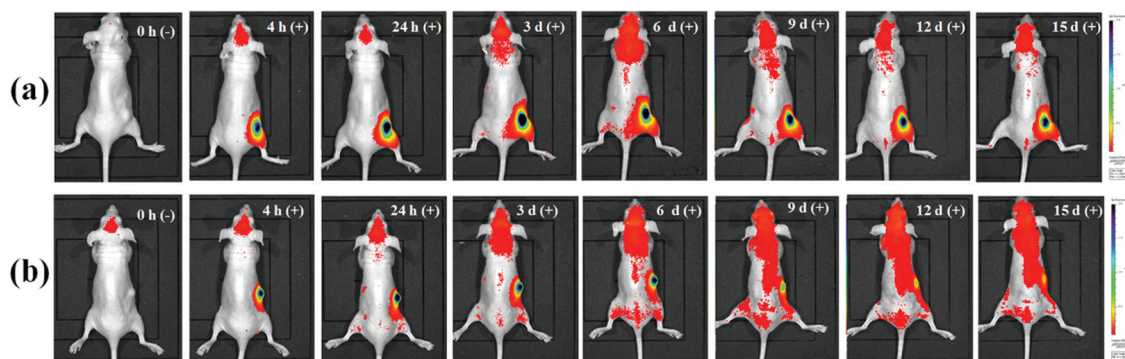By modeling MCF-7 tumor-bearing nude mice, the *in vivo* PDT performance was assessed in all four groups of PBS, PBS

Fig. 7 *In vivo* fluorescence imaging over 15 day treatments of MCF-7 tumor-bearing nude mice in groups of injecting intratumorally FA-NPs-PS and injecting intratumorally FA-NPs-PS + PDT under the irradiation of a 980 nm laser. (a) Fluorescent imaging of MCF-7 tumor-bearing nude mice injected intratumorally with FA-NPs-PS; (b) fluorescent imaging of MCF-7 tumor-bearing nude mice injected intratumorally with FA-NPs-PS and irradiated with a 980 nm laser for PDT.
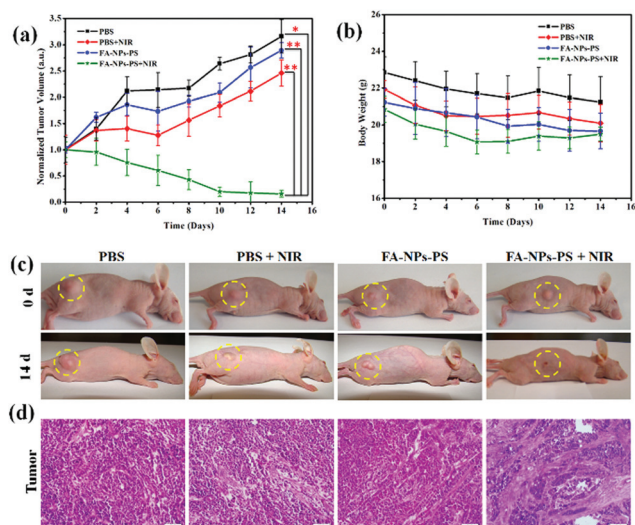
Fig. 8 *In vivo* PDT characterization of MCF-7 tumor-bearing nude mice in different groups of PBS, PBS + NIR, FA-NPs-PS, and FA-NPs-PS + NIR. (a) The change of relative tumor volume of MCF-7 tumor-bearing nude mice in different groups (*$p < 0.05$, **$p < 0.01$); (b) the change of body weight of MCF-7 tumor-bearing nude mice in different groups; (c) the real photographs of MCF-7 tumor-bearing nude mice in different groups at the beginning and at the end of the 15 day treatments; and (d) H&E staining images of tumors in different groups (the scale bar is 50 μm).

Fig. 9 H&E staining images of major organs (heart, liver, spleen, lung, and kidney) of MCF-7 tumor-bearing nude mice in groups of PBS, PBS + NIR, FA-NPs-PS, and FA-NPs-PS + NIR (the scale bar is 50 μm).

+ NIR, FA-NPs-PS and FA-NPs-PS + NIR. Fig. 8(a) and (b) show the change in relative tumor volume and body weight of MCF-7 tumor-bearing nude mice over 15 day treatments. On the final day, the relative volume of the MCF-7 tumors was 3.16, 2.46, and 2.89 in groups of PBS, PBS + NIR, FA-NPs-PS, but was only 0.16 in the group of FA-NPs-PS + NIR. Moreover, the body weight in all four groups did not evidently decrease. Fig. 8(c) gives the real images of MCF-7 tumor-bearing nude mice in all four groups at the beginning and at the end of the 15 day treatments, in which the tumor volume in the group of FA-NPs-PS + NIR almost disappeared after the 15 day treatment. Furthermore, histological analysis of the tumors was also characterized. Fig. 8(d) shows H&E staining images of the tumors in all four groups, in which many apoptotic and necrotic tumor cells appeared in the group of FA-NPs-PS + NIR, but not nearly in other groups. The results demonstrated that MCF-7 tumors could be treated by NIR-triggered PDT of FA-NPs-PS nanocomposites.

In order to assess the effect of FA-NPs-PS nanocomposites and NIR irradiation on tumor treatment, the tissue sections of the major organs (heart, liver, spleen, lung, and kidney) of MCF-7 tumor-bearing nude mice in four groups were analyzed by H&E staining. As shown in Fig. 9, in all four groups, the fibrosis in the heart and lung samples was not detected, the inflammatory reaction in the liver section was not found, and the glomerular and tubular structures in the kidney samples were also clearly displayed. Histological analysis of major organs revealed that pathological changes were not found in any histological specim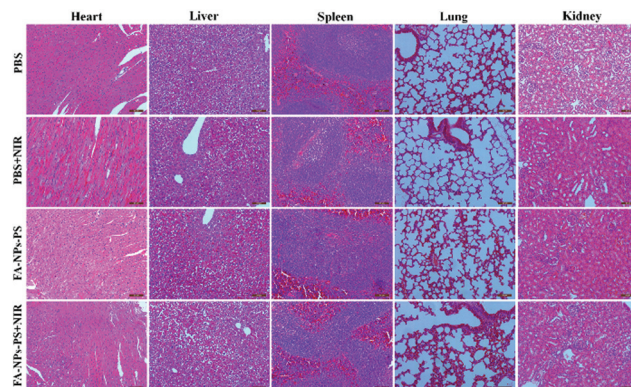ens of all four groups. Therefore, these results demonstrate the safety and the potential clinical application of FA-NPs-PS nanocomposites in MRI and NIR-triggered PDT of breast cancers.

4. Conclusions

In summary, FA-targeted, PS-loaded Fe_3O_4@$NaYF_4$:Yb/Er nanocomposites were synthesized for *in vivo* T_2-weighted MRI and NIR-triggered PDT in deep-tissue tumors. The as-prepared FA-NPs-PS nanocomposites showed low cytotoxicity and good biocompatibility *in vitro* and *in vivo*. Moreover, the fluorescence tracing of FA-NPs-PS nanocomposites in cells and in tumors demonstrated the effective targeting ability of FA *in vitro* and *in vivo*. Under the irradiation of a 980 nm laser, the viabilities of MCF-7 and HeLa cells decreased to about 18.4% and 30.7%, and the relative volume of the MCF-7 tumor decreased to about 0.16, which indicated an excellent NIR-triggered PDT performance. The MR measurement showed a transverse relaxivity value (r_2) of 63.79 mM^{-1} s^{-1}, and *in vivo* MR images demonstrated the application in T_2-weighted MR contrast agents. These results provide useful information about the reliability of FA targeting and *in vivo* MRI/PDT performance and will be important to the probable application of FA-NPs-PS nanocomposites in MRI diagnosis and visualized PDT of deep-tissue cancers later, including breast cancer.

Acknowledgements

Notes and references

1 P. Huang, J. Lin, X. Wang, Z. Wang, C. Zhang, M. He, K. Wang, F. Chen, Z. Li, G. Shen, D. Cui and X. Chen, *Adv. Mater.*, 2012, **24**, 5104–5110.

2 B. Jang, J. Y. Park, C. H. Tung, I. H. Kim and Y. Choi, *ACS Nano*, 2011, **5**, 1086–1094.

3 J. Lin, S. Wang, P. Huang, Z. Wang, S. Chen, G. Niu, W. Li, J. He, D. Cui, G. Lu, X. Chen and Z. Nie, *ACS Nano*, 2013, **7**, 5320–5329.

4 G. Gollavelli and Y. C. Ling, *Biomaterials*, 2014, **35**, 4499–4507.

5 D. Ling, W. Park, S. Park, Y. Lu, K. S. Kim, M. Hackett, B. H. Kim, H. Yim, Y. S. Jeon, K. Na and T. Hyeon, *J. Am. Chem. Soc.*, 2014, **136**, 5647–5655.

6 D. Wang, B. Fei, L. Halig, X. Qin, Z. Hu, H. Xu, Y. A. Wang, Z. Chen, S. Kim, D. Shin and Z. Chen, *ACS Nano*, 2014, **8**, 6620–6632.

7 Y. Ma, S. Tong, G. Bao, C. Gao and Z. Dai, *Biomaterials*, 2013, **34**, 7706–7714.

8 H. Gong, Z. Dong, Y. Liu, S. Yin, L. Cheng, W. Xi, J. Xiang, K. Liu, Y. Li and Z. Liu, *Adv. Funct. Mater.*, 2014, **24**, 6492–6502.

9 P. Huang, Z. Li, J. Lin, D. Yang, G. Gao, C. Xu, L. Bao, C. Zhang, K. Wang, H. Song, H. Hu and D. Cui, *Biomaterials*, 2011, **32**, 3447–3458.

10 M. Lin, Z. Li, Z. Liu, J. Ren, X. Yang and X. Qu, *Chem. Commun.*, 2012, **48**, 6556–6558.

11 X. Liang, X. Li, L. Jing, X. Yue and Z. Dai, *Biomaterials*, 2014, **35**, 6379–6388.

12 Z. Li, C. Wang, L. Cheng, H. Gong, S. Yin, Q. Gong, Y. Li and Z. Liu, *Biomaterials*, 2013, **34**, 9160–9170.

13 J. Shi, L. Wang, J. Gao, Y. Liu, J. Zhang, R. Ma, R. Liu and Z. Zhang, *Biomaterials*, 2014, **35**, 5771–5784.

14 L. Zeng, W. Ren, L. Xiang, J. Zheng, B. Chen and A. Wu, *Nanoscale*, 2013, **5**, 2107–2113.

15 J. V. Frangioni, *Curr. Opin. Chem. Biol.*, 2003, **7**, 626–634.

16 S. S. Lucky, N. M. Idris, Z. Li, K. Huang, K. C. Soo and Y. Zhang, *ACS Nano*, 2015, **9**, 191–205.

17 R. Wang and F. Zhang, *J. Mater. Chem. B*, 2014, **2**, 2422–2443.

18 S. Cui, D. Yin, Y. Chen, Y. Di, H. Chen, Y. Ma, S. Achilefu and Y. Gu, *ACS Nano*, 2013, **7**, 676–688.

19 J. Y. Yhee, S. Lee and K. Kim, *Nanoscale*, 2014, **6**, 13383–13390.

20 P. Huang, C. Xu, J. Lin, C. Wang, X. Wang, C. Zhang, X. Zhou, S. Guo and D. Cui, *Theranostics*, 2011, **1**, 240–250.

21 S. Cui, D. Yin, Y. Chen, Y. Di, H. Chen, Y. Ma, S. Achilefu and Y. Gu, *ACS Nano*, 2013, **7**, 676–688.

22 L. Xia, X. Kong, X. Liu, L. Tu, Y. Zhang, Y. Chang, K. Liu, D. Shen, H. Zhao and H. Zhang, *Biomaterials*, 2014, **35**, 4146–4156.

23 D. Yang, X. Kang, P. Ma, Y. Dai, Z. Hou, Z. Cheng, C. Li and J. Lin, *Biomaterials*, 2013, **34**, 1601–1612.

24 C. Yang, Q. Liu, D. He, N. Na, Y. Zhao and J. Ouyang, *Analyst*, 2014, **139**, 6414–6420.

25 Y. Liu, D. Tu, H. Zhu and X. Chen, *Chem. Soc. Rev.*, 2013, **42**, 6924–6958.

26 J. Zhou, Q. Lu, W. Feng, Y. Sun and F. Li, *Chem. Rev.*, 2015, **115**, 395–465.

27 X. Li, D. Zhao and F. Zhang, *Theranostics*, 2013, **3**, 292–305.

28 C. Liu, Z. Gao, J. Zeng, Y. Hou, F. Fang, Y. Li, R. Qiao, L. Shen, H. Lei, W. Yang and M. Gao, *ACS Nano*, 2013, **7**, 7227–7240.

29 F. Zhang, G. Braun, A. Pallaoro, Y. Zhang, Y. Zhang, D. Cui, M. Moskovits, D. Zhao and G. Stucky, *Nano Lett.*, 2012, **12**, 61–67.

30 H. Zhu, J. Tao, W. Wang, Y. Zhou, P. Li, Z. Li, K. Yan, S. Wu, K. Yeung, Z. Xu, H. Xu and P. Chu, *Biomaterials*, 2013, **34**, 2296–2306.

31 L. Cheng, K. Yang, Y. Li, X. Zeng, M. Shao, S. Lee and Z. Liu, Multifunctional nanoparticles for upconversion luminescence/MR multimodal imaging and magnetically targeted photothermal therapy, *Biomaterials*, 2012, **33**, 2215–2222.

32 L. Zeng, L. Xiang, W. Ren, J. Zheng, T. Li, B. Chen, J. Zhang, C. Mao, A. Li and A. Wu, *RSC Adv.*, 2013, **3**, 13915–13925.

33 L. Zhang, L. Zeng, Y. Pan, S. Luo, W. Ren, A. Gong, X. Ma, H. Liang, G. Lu and A. Wu, *Biomaterials*, 2015, **44**, 82–90.

34 X. Qiao, J. Zhou, J. Xiao, Y. Wang, L. Sun and C. Yan, *Nanoscale*, 2012, **4**, 4611–4623.

35 Y. Zhang, G. Das, V. Vijayaragavan, Q. Xu, P. Padmanabhan, K. Bhakoo, S. Selvan and T. Tan, *Nanoscale*, 2014, **6**, 12609–12617.

36 F. Chen, S. Zhang, W. Bu, Y. Chen, Q. Xiao, J. Liu, H. Xing, L. Zhou, W. Peng and J. Shi, *Chem. – Eur. J.*, 2012, **18**, 7082–7090.

37 Y. Park, H. M. Kim, J. H. Kim, K. C. Moon, B. Yoo, K. T. Lee, N. Lee, Y. Choi, W. Park, D. Ling, K. Na, W. K. Moon, S. H. Choi, H. S. Park, S. Y. Yoon, Y. D. Suh, S. H. Lee and T. Hyeon, *Adv. Mater.*, 2012, **24**, 5755–5761.

38 G. Liu, J. Gao, H. Ai and X. Chen, *Small*, 2013, **9**, 1533–1545.

39 B. Liu, C. Li, P. Ma, Y. Chen, Y. Zhang, Z. Hou, S. Huang and J. Lin, *Nanoscale*, 2015, **7**, 1839–1848.

40 X. Zhu, J. Zhou, M. Chen, M. Shi, W. Feng and F. Li, *Biomaterials*, 2012, **33**, 4618–4627.

41 D. Hu, M. Chen, Y. Gao, F. Li and L. Wu, *J. Mater. Chem.*, 2011, **21**, 11276–11282.

42 C. Mi, J. Zhang, H. Gao, X. Wu, M. Wang, Y. Wu, Y. Di, Z. Xu, C. Mao and S. Xu, *Nanoscale*, 2010, **2**, 1141–1148.